Journal of Luminescence 231 (2021) 117837

Contents lists available at ScienceDirect

Journal of Luminescence

journal homepage: http://www.elsevier.com/locate/jlumin

Large-area luminescent solar concentrator utilizing donor-acceptor luminophore with nearly zero reabsorption: Indoor/outdoor performance evaluation

Fahad Mateen [a], Yilin Li [b], Muhammad Ahsan Saeed [c], Yujian Sun [d], Yongcao Zhang [e], Sae Youn Lee [f], Sung-Kyu Hong [a,*]

[a] Department of Chemical and Biochemical Engineering, Dongguk University, Seoul, 04620, Republic of Korea
[b] Department of Chemical and Biomolecular Engineering, Rice University, Houston, TX, 77005, United States
[c] Department of Electronics and Electrical Engineering, Dongguk University, Seoul, 04620, Republic of Korea
[d] School of Environmental and Forest Sciences, University of Washington, Seattle, WA, 98195, United States
[e] Department of Mechanical Engineering, University of Houston, Houston, TX, 77004, United States
[f] Department of Energy and Material Engineering, Dongguk University, Seoul, 04620, Republic of Korea

ARTICLE INFO

Keywords:
Luminescent solar concentrator
Large Stokes shift
Intramolecular charge transfer
Indoor/outdoor illumination
Aesthetics

ABSTRACT

Luminescent solar concentrators (LSCs) are light-guides doped with luminophores that can spectrally and spatially concentrate solar radiation. With the ability to harvest both direct and diffuse light, LSCs are considered attractive prospects for building-integrated photovoltaic applications. However, it is still challenging to develop organic luminophores based large-area LSCs that work well in various illumination conditions. Reabsorption, caused by small stokes shift of typical organic luminophores, often limits the performance of large-area LSCs. This study reports an indoor and outdoor performance of large-area ($\geq$100 cm^2) LSCs that employ a donor-acceptor luminophore with a large Stokes shift. The largest (400 cm^2) LSC demonstrates an optical efficiency (η_{opt}) of 5.5% and 7.6% under outdoor (AM 1.5G) and indoor (white LED) illuminations, respectively. Furthermore, the aesthetic and visual comfort parameters such as chromaticity coordinates, color rendering index, and average visible transmission are obtained that suggest the suitability of our LSCs for a built environment.

1. Introduction

Luminescent solar concentrators (LSCs) are photonic devices that harvest sunlight over a large surface area to generate electricity and can be easily implemented as building integrated photovoltaic (BIPV) elements [1,2]. Typically, an LSC consists of transparent glass or polymer slab infused or coated with highly emissive luminophores. Following absorption of incoming solar photons impinging onto a larger surface of the slab, luminophores re-emit photons at longer wavelengths, and a fraction of the re-emitted photons are guided by total internal reflection to the LSC edges where they are converted into electricity by the attached PV cells (Fig. 1a) [3–5]. Simple architecture, tunable colors, and the ability to concentrate both direct and diffuse light allows LSCs to be incorporated into diverse locations such as building windows, facade claddings, and greenhouse panels [6,7].

Despite huge potential, the LSC technology is still facing some challenges such as reabsorption loss [8–10], limited photostability [11–13], and low photoluminescence quantum yield (PLQY) of luminophores [14,15]. The reabsorption loss that occurs due to a large overlap between the absorption and emission spectra of luminophore is the most crucial in determining the performance of large-area LSCs [16–18]. When multiple reabsorption events occur, an extra loss mechanism (e.g., escape-cone loss) can be introduced, which would further reduce device performance. Significant research efforts have been dedicated to deal with reabsorption issues. These efforts include the use of large Stokes shift dyes [19], aggregation-induced emissions (AIE) dyes [20,21], donor-acceptor (D-A) energy transfer [22–26], inorganic quantum dots (QDs) [27–31], and tandem structures [32–34]. Recently, we proposed single molecule D-A thermally activated delayed fluorescence (TADF) dyes for LSC applications.

* Corresponding author.
E-mail address: hsk5457@dongguk.edu (S.-K. Hong).

https://doi.org/10.1016/j.jlumin.2020.117837
Received 14 August 2020; Received in revised form 2 December 2020; Accepted 3 December 2020
Available online 5 December 2020

Most of the studies have been restricted to relatively small-area (<60 cm^2) LSCs as they are easy to fabricate [35–39]. To date, the highest reported power conversion efficiency (η_{PCE}) is 7.1% [40], which was achieved through an energy-transfer-based 5 × 5 cm^2 LSC using a green naphthalene dye and a red perylene dye, and a high-efficiency (>25%) gallium arsenide PV cells under AM 1.5G spectrum. With silicon PV cells, the highest η_{PCE} reported to date is 4.2% for a 5 × 5 cm^2 device [41]. All these results were achieved by using a back-reflector to the LSC. Nevertheless, smaller LSCs are sufficient for investigating the fundamental aspects, large-area LSCs are logically more appropriate for dealing with the challenges that arise from the upscaling of the LSC technology especially for the built environment. Targeting large-area LSCs, Meinardi et al. fabricated a 12 × 12 cm^2 LSC based on near-infrared (NIR) $CuInSeS_2$/ZnS QDs, and the device exhibited an optical efficiency (η_{opt}) of 3.2% [42]. Subsequently, the same group developed a 12 × 12 cm^2 LSC (η_{PCE} = 2.8%) based on NIR silicon QDs [6]. Few other reports regarding large-area LSCs include tandem LSCs employing green carbon and perovskite QDs (10 × 10 cm^2, η_{opt} = 3.0%) [32], thin-film LSCs coated with red silica encapsulated CdSe/CdS QRs (15 × 15 cm^2, η_{opt} = 2.2%) [43], LSCs based on NIR $CuInS_2$/ZnS QDs (10 × 10 cm^2, η_{PCE} = 2.9% and η_{opt} = 8.1%) [44], carbon QDs doped LSC (15 × 15 cm^2, η_{opt} = 2.2%) [45] and glass laminated LSCs employing red perylene dye (31.2 × 31.2 cm^2, η_{PCE} = 0.98%) [46]. Unlike inorganic QDs, traditional organic dyes show better PLQY and less concentration quenching in polymers, yet their applicability in large-area LSC is limited as they exhibit small stokes shifts and more reabsorption losses. Moreover, a major portion of the LSC research is focused on performance under outdoor conditions i.e. air mass (AM) 1.5 global(G) spectrum, while there are few reports on LSC under indoor light conditions [47]. LSCs in outdoor conditions perform differently from those in an indoor environment due to varied spectrum and intensities.

This study investigates the indoor and outdoor performance of low reabsorbing large-area (≥100 cm^2) LSCs utilizing large Stokes shift TADF dye, 1,2,3,5 tetrakis(carbazol-9-yl)-4,6-dicyanobenzene (4CzIPN). 4CzIPN is a carbazoledicyanobenzene (CDCB)-based TADF dye with electron-rich carbazole (Cz) as the charge donor and electron-deficient dicyanobenzene (CB) as the charge acceptor (Fig. 1b). Intramolecular charge transfer (ICT) between the Cz and CB moiety causes a drastic increase in the Stokes shift. Low reabsorption loss, high photostability due to strong steric hindrance, and high PLQY of 4CzIPN allow it to be an excellent candidate for the development of large-area LSCs. We initially synthesized 4CzIPN (details included in the experimental section) and subsequently, LSCs of different sizes (surface area up to 20 × 20 cm^2) were fabricated by embedding 4CzIPN in poly(methyl methacrylate) (PMMA). Additionally, we performed the aesthetic analysis of 4CzIPN-doped LSC devices, which has not been reported previously.

2. Experimental

2.1. Materials

For the synthesis of 4CzIPN, all reagents were purchased from Sigma Aldrich, Tokyo Chemical Industry (TCI), and Wako Pure Chemical Industries. Methyl methacrylate (MMA) and azobisisobutyronitrile (AIBN) for the LSC fabrication were purchased from Sigma Aldrich.

2.2. Synthesis of 4CzIPN

60% sodium hydride (0.94 g, 39 mmol) was washed with hexane and dissolved in anhydrous tetrahydrofuran (100 mL) under nitrogen atmosphere at 0 °C followed by the addition of 9*H*-carbazole. The mixture

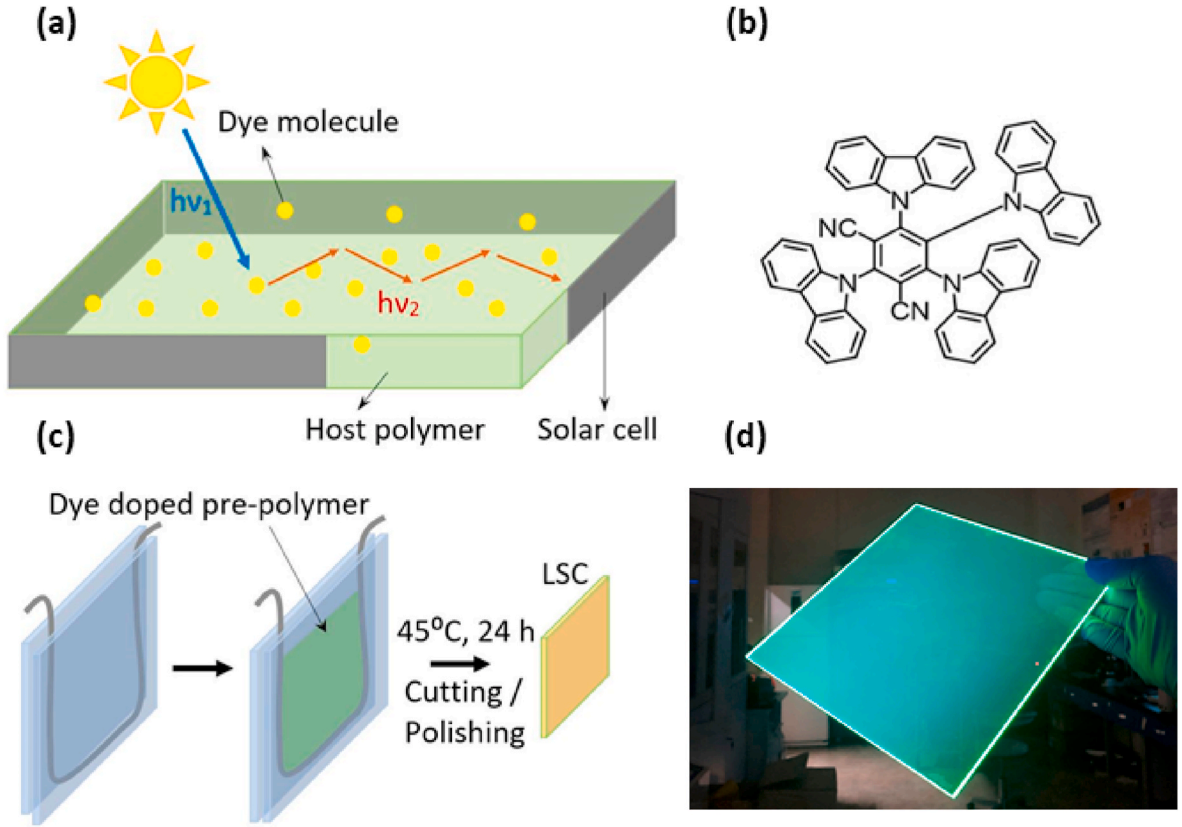

Fig. 1. (a) Schematic representation of an LSC attached to solar cells. The fraction of solar photons (hv_1) is absorbed by the dye molecules and is re-emitted at longer wavelengths. Re-emitted photons (hv_2) are guided towards the edges of the LSC via total internal reflection, where they are converted into electricity using attached solar cells. (b) Molecular structure of 4CzIPN. (c) A fabrication process of the LSCs. (d) Photograph of a 4CzIPN-doped LSC illuminated with a light at 365 nm.

was then stirred for 30 min and cooled down to room temperature. After 1 h, 2,4,5,6- tetrafluoroisophthalonitrile (0.52 g, 2.6 mmol) was added at 0 °C. After 30 min, the mixture was stirred at room temperature overnight. The organic layer was then washed with water and dried over anhydrous magnesium sulfate. The crude product was purified by column chromatography on silica gel (hexane/acetone = 1:2, *v/v*) to obtain 4CzIPN as a yellow powder (yield = 75%). The reaction for the synthesis of 4CzIPN is shown in supporting information Fig. S1. ^{1}H NMR (500 MHz, $CDCl_3$): δ = 8.23 (d, J = 7.7 Hz, 2H), 7.73–7.67 (m, 8H), 7.49 (td, J = 7.9, 1.3 Hz, 2H), 7.34 (d, J = 7.4 Hz, 2H), 7.23 (dd, J = 7.2, 1.2 Hz, 4H), 7.11–7.05 (m, 8H), 6.82 (t, J = 7.8 Hz, 4H), 6.63 (td, J = 7.9, 1.1 Hz, 2H).

2.3. Fabrication of LSCs

The LSCs were fabricated according to the method reported previously [48]. First, 0.1 w/w% AIBN (Aldrich, USA) and 0.03 w/w% of 4CZIPN were mixed with MMA, followed by sonication for 15 min. The mixture was heated to 85 °C to initiate the free-radical polymerization reaction. After 30–45 min, the solution turned into a viscosity liquid, indicating the formation of the prepolymer. After that, the mixture was cooled to room temperature and poured into a glass mold. The resulting product was dried in the mold at 45 °C for 24 h. Finally, the 4CzIPN--doped PMMA was laser-cut into square pieces of required dimensions and further polished to obtain the 0.3 cm thick LSCs (Fig. 1c).

2.4. Measurements

Absorption and emission spectra were measured using UV–visible (UV–vis) spectrophotometer (PerkinElmer Lambda 35) and fluorescence spectrophotometer (JASCO, FP-8600), respectively. NMR spectrum of the synthesized 4CzIPN was recorded on an Avance III 500 spectrometer (Bruker), using tetramethylsilane (δ = 0.00) as an internal standard. For PV measurements, crystalline silicon (c-Si) PV cells purchased from Puguang Solar China were employed. Optically transparent refractive index matching epoxy adhesive (United Adhesives, OE 1582) was used to bind the solar cells with all edges of the LSCs. For outdoor conditions, the IV measurements were taken by illuminating the LSC surface with a solar simulator (Mc-Science) having a Xenon arc lamp of 160 W equipped with filters to approximate AM 1.5G spectrum. The power density was calibrated before performing the efficiency tests and found to be 100 mW cm^{-2}. For the evaluation in the indoor environment, a light-emitting diode (LED) lamp (SLS LED100, McScience, Republic of Korea) with an irradiance of 0.28 mW cm^{-2} (at 1000 lux) was used for illumination. International Commission on Illumination (CIE) 1931 chromaticity coordinates (x,y) and spectral analysis of transmitted light were obtained by using a spectrometer (Avantes, ULS2048).

3. Result and discussion

The solid matrix has numerous impacts on the photophysical properties of doped luminophores, which are directly related to LSC operations, such as transparency, solid-state PLQYs, and photostability. Therefore, all the photophysical properties of 4CzIPN were obtained in solid PMMA (actual LSC device) rather than in solution form. The normalized absorption spectrum of 4CzIPN and irradiance of LED light and AM 1.5G spectra are displayed in Fig. 2a. The absorption spectrum shows two prominent peaks with a band edge at about 500 nm, suggesting that 4CzIPN can absorb the sunlight with a wavelength range from 300 to 500 nm. Based on the absorption spectrum of 4CzIPN, we calculated the absorption efficiency of the LSC device using Eq. (1).

$$\eta_{abs} = \frac{(1-R)\int_{300}^{1100} P_{in}(\lambda)\,[1-e^{-\alpha(\lambda)t}]d\lambda}{\int_{300}^{1100} P_{in}(\lambda)d\lambda} \quad (1)$$

where R represents the reflection losses which are approximately 4% in

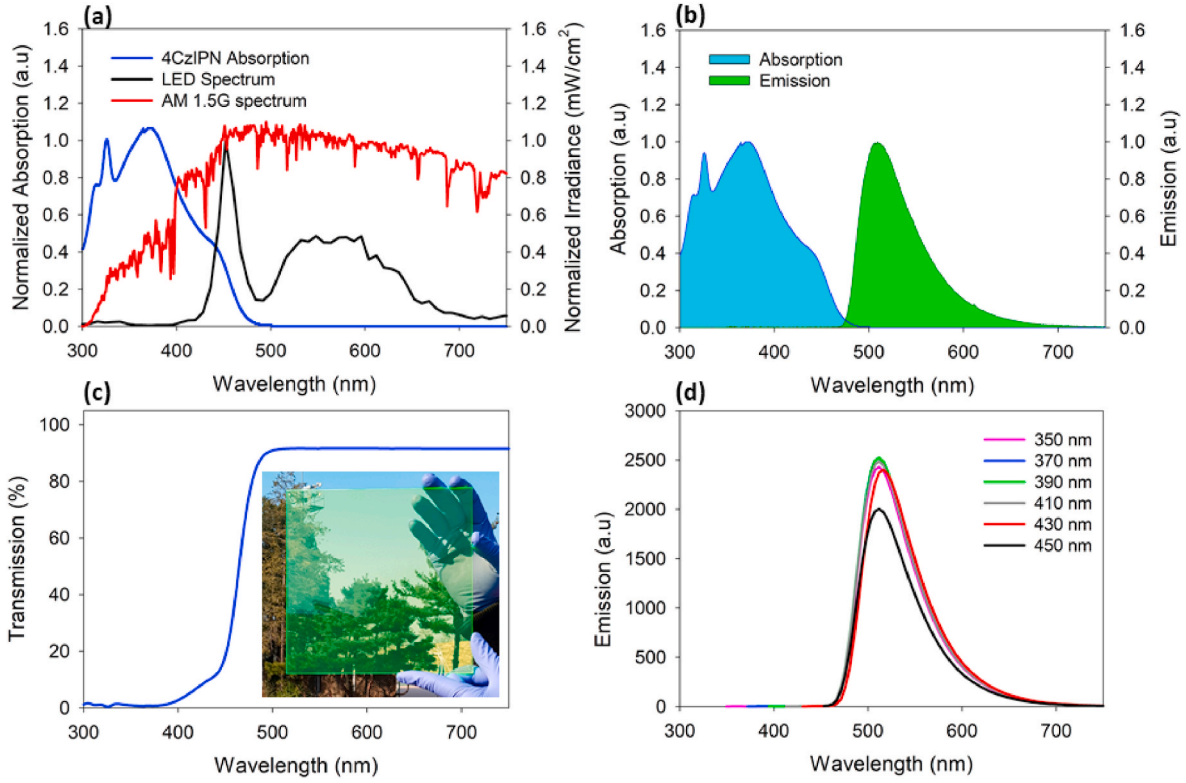

Fig. 2. (a) Absorption spectrum of 4CzIPN and the LED light and AM 1.5G irradiance spectra. (b) Absorption and emission spectra of 4CzIPN-doped LSC. (c) Transmission spectrum and a photograph of 4CzIPN-doped LSC (20 × 20 cm2) under direct sunlight (insert). (d) Emission spectra of the same LSC at various excitation wavelengths. The concentration of 4CzIPN in all measurements were kept at 0.03 wt/wt%.

the case of air/PMMA system, α is the absorption coefficient, t is the thickness of the LSC, and P_{in} is the incident photon flux. According to Eq. (1), η_{abs} of 4CzIPN-doped LSC was found to be ~12.5% and ~16% for AM 1.5G and LED light, respectively before the bandgap of Si ($E_g = 1.1$ eV or 1100 nm). As shown in Fig. 3b, there is a negligible overlapping of absorption and emission spectra of 4CzIPN. The emission spectrum of the 4CzIPN exhibits a single peak with the maximum value at 509 nm and a full width at half maximum (FWHM) of ~65 nm. Stokes shift defined by the difference between absorption and emission maxima ($\lambda_{em.max.} - \lambda_{abs.max.}$) is 139 nm and is significantly larger than that of first-generation organic fluorophores [49,50]. Such a large stoke shift is attributed to the ICT characteristics and twisted structures of 4CzIPN resulted from the steric hindrance [51]. Fig. 2c shows the transmittance spectrum of 4CzIPN-doped LSC as well as a photograph of this device under direct sunlight in the inset. As can be seen, the LSC shows very high transmittance (~92%) in the wavelength range from 500 to 750 nm, implying a good optical quality of the device. Moreover, due to the strong absorption at shorter wavelengths from 300 to 500 nm, a drastic decrease in transmittance in this range (~0% at 350 nm) is particularly notable. To further investigate the photophysical properties of the 4CzIPN-doped LSC, the emission spectra were assessed at different excitation wavelengths. As shown in Fig. 2d, variation in emission intensity and FWHM are negligible when the excitation wavelength is changed from 350 nm to 430 nm. However, a slight decrease in emission intensity is observed at 450 nm. This emission behavior suggests that the 4CzIPN-doped LSC can actively harvest photons in the entire absorption range. We also obtained the PLQY of 4CzIPN using an integrating sphere method. In general, 4CzIPN shows very high PLQY (~94%) in toluene solution [51]. While, in solid-state PMMA, we obtained the lowest PLQY (67.8%) at 330 nm and the highest (68.1%) at 440 nm. The average PLQY calculated in the given range was 67%. Reduced PLQY in solid-state can be due to the fact that solid PMMA locks the molecular conformation of the dye, and in this molecular conformation, the dye lacks the excitation relaxation process and more non-radiative decay happens.

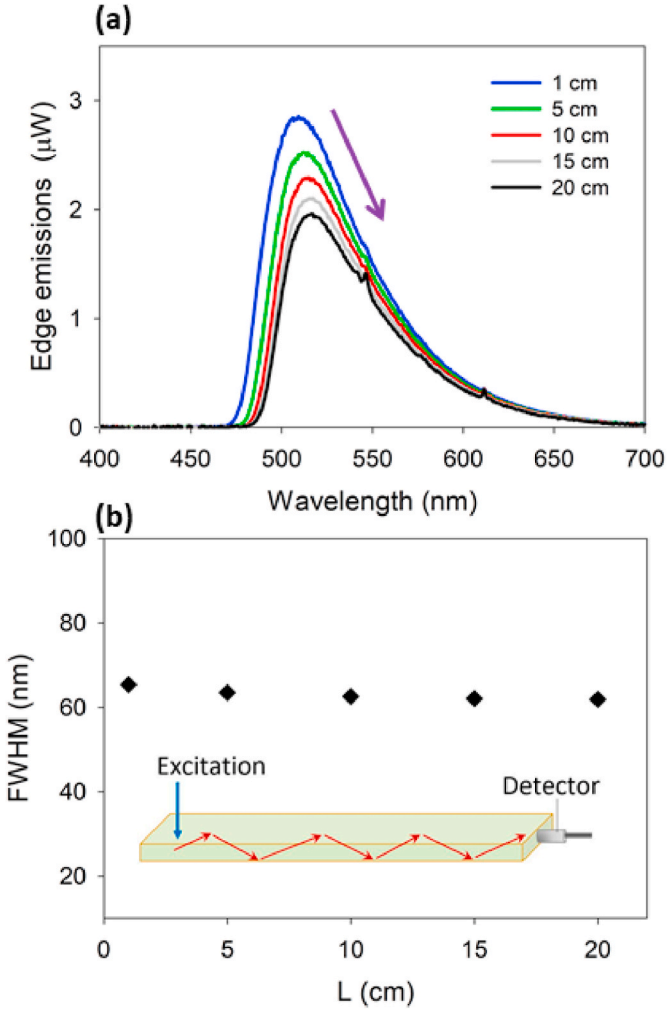

Fig. 3. (a) Edge emission spectra of the 4CzIPN-doped LSC collected at increasing optical distance, L, between the excitation spot and the edge of a long-length 4CzIPN-doped LSC (excitation wavelength = 365 nm; dimensions: 30 × 3 × 0.3 cm^3; 4CzIPN concentration: 0.03 wt/wt %) (b) Variation in FWHM with the increasing L.

To experimentally evaluate the loss channels, particularly reabsorption loss in the 4CzIPN-doped LSCs, we fabricated a long-length LSC and collected the emission spectra using a monochromatic excitation source (365 nm) positioned at various optical distances (L) from the photodetector attached to its shorter edge (Insert Fig. 3b). As expected, a slight decrease in edge emission was observed resulting in ~23% intensity loss at 10 cm optical distance, reaching ~35% dimming for L = 20 cm (Fig. 3a). Given a small overlap between absorption and emission spectra of 4CzIPN, such dimming in the emission spectra with increasing L suggests the presence of other loss channels (e.g., scattering loss, matrix absorption). Further, with the increasing L, we also observe a slight decrease in FWHM towards a higher wavelength (Fig. 3b).

We first obtained the outdoor performance of the 4CzIPN-doped large-area LSCs. For the purpose, we fabricated square-shaped LSCs with a constant thickness ($t = 0.3$ cm): LSC-1 (10 × 10 cm^2), LSC-2 (15 × 15 cm^2), and LSC-3 (20 × 20 cm^2). After connecting with Si PV cells, the LSCs were illuminated using a calibrated light source (AM 1.5 G, power density $I = 100$ mW cm^{-2}), and current-voltage (IV) measurements were performed (1) without and (2) with a white backside diffuser. The scheme of Si PV cell connection and IV curves have been shown in Fig. S2 and Fig. S3 of supporting information. Without the backside diffuser, less current was generated but optical transmittance of the devices was preserved to reproduce the situation of light-harvesting building windows. On the contrary, the use of a white backside diffuser helped to recycle transmitted and emitted photons escaping from the rear side of LSCs, therefore, the current generation was high. Such devices can be applied to architectural positions other than windows.

Figures-of-merits for the LSCs and their respective definitions vary between laboratories, thus complicates the comparison between the literature. Herein, we have used optical efficiency (η_{opt}) and concentration gain factor (C^*) to evaluate the performance of our devices. η_{opt} is defined as a ratio of photons emitted from LSC edges to the photons incident on its surface and is calculated using Eq. (2) [27,52,53].

$$\eta_{opt} = \frac{I_{LSC} \times A_{Edges}}{I_{PV} \times A_{LSC}} = \frac{I_{LSC}}{I_{SC} \times G} \quad (2)$$

$$C^* = \eta_{opt} \times G \quad (3)$$

where I_{LSC} is the short circuit current produced by the PV cells coupled to the LSC, and I_{PV} is the short circuit current of the PV cells under direct illumination. G is the geometric factor defined as the ratio of the surface area of an LSC to the area of its edges where PV cells are attached (A_{LSC}/A_{Edges}), and it significantly affects the η_{opt} of the device. Among the fabricated devices, a maximum η_{opt} was shown by LSC-1 (G = 8.3), for example, 5.2% and 7.7% without and with the backside diffuser, respectively. On the other hand, the minimum η_{opt} was observed in the case of LSC-3 (G = 16.6). As of Eq. (3), C* increases with increasing LSC area, therefore, the highest and the lowest C^* was shown by LSC-3 and LSC-1, respectively (Table 1).

To validate the experimental output, a Monte Carlo ray-tracing simulation was also performed according to the literature [54–56]. The results demonstrate that simulated η_{opt} of LSC-1, LSC-2, and LSC-3

Table 1
Experimental optical efficiency (η_{opt}) and concentration factor (C*) of large-area LSCs under outdoor (AM 1.5G) and indoor (LED) illuminations.

Sample	η_{opt}	C*
Without backside diffuser (Under AM 1.5 G)		
LSC-1 (G = 8.3)	5.2	0.4
LSC-2 (G = 12.5)	4.4	0.5
LSC-3 (G = 16.6)	3.7	0.6
With backside diffuser (Under AM 1.5 G)		
LSC-1 (G = 8.3)	7.7	0.6
LSC-2 (G = 12.5)	6.8	0.8
LSC-3 (G = 16.6)	5.5	0.9
With backside diffuser (Under LED)		
LSC-1 (G = 8.3)	12.6	1.0
LSC-2 (G = 12.5)	9.4	1.2
LSC-3 (G = 16.6)	7.6	1.3

without a backside diffuser are 5.3, 4.9, and 3.8%, respectively, and are in good agreement with the experimentally observed values (Fig. 4a and (b)). Additionally, we employed the experimental device parameters (dimensions, absorption, and emission spectra, PLQY) to further estimate the optical performances potentially achievable for the LSCs with an increasingly larger area (up to 2500 cm^2). According to the simulation results, with increasing the LSC area (without backside diffuser) to 2500 cm^2 (G = 42), η_{opt} decreases to ~2% and C* increases to ~0.9 (Fig. 4a). While, with the backside diffuser, an LSC with the same dimensions exhibits simulated η_{opt} and C* of ~2.7% and ~1.1, respectively (Fig. 4b). The rise in C* for large areas is consistent with the edge photon flux represented in Fig. 4d. On the other hand, reduction of η_{opt} is expected with the increasing area since large-area LSCs suffer from greater optical losses (e.g., weak reabsorption near the band edge of 4CzIPN, scattering loss, and PMMA matrix loss) due to longer path-lengths that photons are required to travel before reaching the edge-mounted PV cells. Another feature of Fig. 4b) is that η_{opt} drop is more rapid for small areas, for example, η_{opt} drops from 7.7% to 3.5% (~54% reduction) when area increases from 1.44 cm^2 (G = 1) to 500 cm^2 (G = 22). While, with increasing area from 500 cm^2 to 2500 cm^2, reduction in η_{opt} is ~42%. Comparing η_{opt} of 4CzIPN-doped LSC to other green emission organic dyes based LSC, we observe that the η_{opt} of the 4CzIPN-doped LSC (area 5 × 5 cm^2, G = 4) is 6.8% which is higher than the recently reported green emission benzo[1,2-*d*:4,5-*d*′]bisthiazole (BBT) heterocyclic luminophore based LSC with the same area [57].

To explore the ultimate performance of 4CzIPN-doped large-area LSCs, we performed simulations with varying PLQY of 4CzIPN (up to 100%). In this regard, we highlight a recent study by Haichuan Mu et al. in which the plasmonic gold nanoparticles have been employed to enhance the emissions and PLQY (73%) of 4CzIPN [58]. As shown in Fig. 4c, for the given LSCs, η_{opt} increases linearly with increasing PLQY from 50 to 100%. With 100% PLQY, LSC-1 (100 cm^2) would exhibit a maximum η_{opt} of 7% and for a 900 cm^2 LSC, η_{opt} would be 4.4%.

Next, we explore the potential of the 4CzIPN-doped LSCs for utilizing under indoor light conditions. Nevertheless, the illumination color and intensity of indoor lights vary according to the building requirements. In this study, we have employed white light LED ($I = 0.28$ mW cm^{-2}, 1000 lux), which is similar to that reported in recent studies for the evaluation of LSC under indoor conditions [47,59]. Fig. 5a reports experimental and simulated results of increasing LSC area (with backside diffuser) on the η_{opt} and C* under indoor LED illumination. IV curves of LSCs under LED illumination are given in Fig. S4 of the supporting information. Surprisingly, large-area LSCs (up to 1474.5 cm^2, G = 32) exhibit higher η_{opt} and C* under LED illumination than that under AM 1.5G

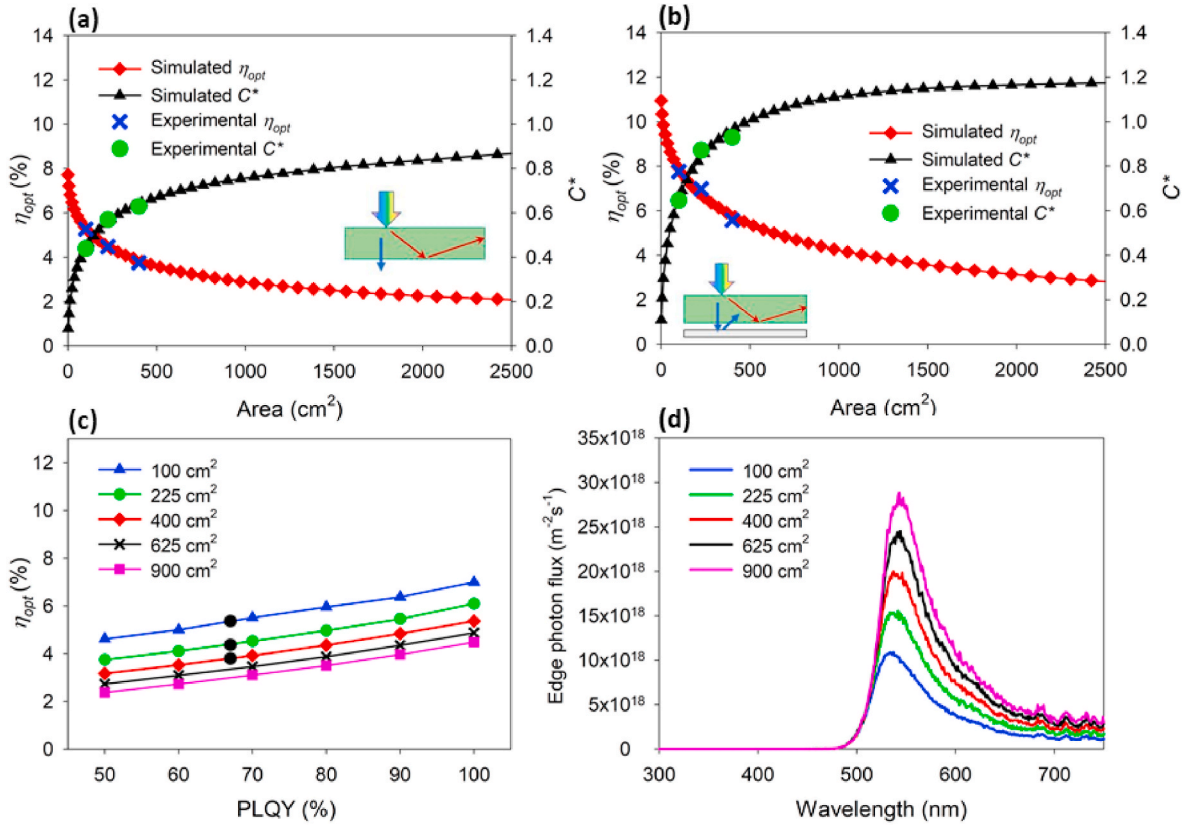

Fig. 4. Performance of the 4CzIPN-doped large-area LSC devices under AM 1.5G solar simulator. Optical efficiency (η_{opt}) and concentration factor (C*) of large-area LSC (a) without and (b) with a backside diffuser (c) Simulated η_{opt} of the large-area LSC devices with the PLQY of 4CzIPN varied from 50% to 100%. Black circles indicate the PLQY of our synthesized 4CzIPN i.e. 67% (d) Simulated photon flux and edge emission spectra of large-area LSC devices. The thickness of all devices is 0.3 cm, while Area = L × W, whereas L = W.

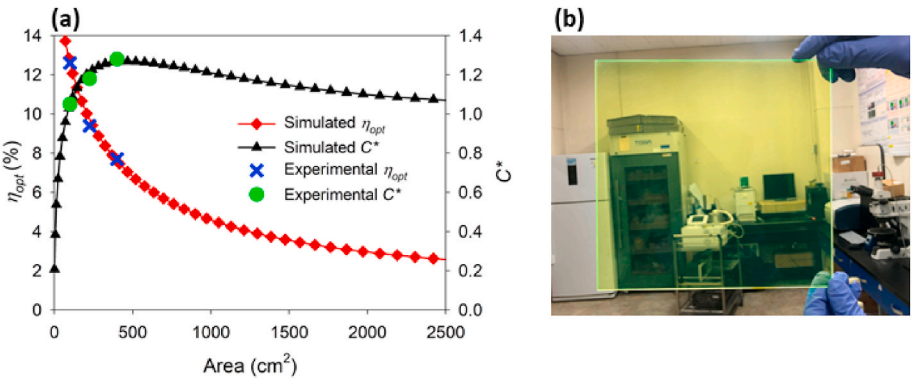

Fig. 5. (a) Optical efficiency (η_{opt}) and concentration factor (C*) of 4CzIPN-doped large-area LSC devices under an indoor LED light. (b) Photograph of 4CzIPN-doped large-area LSC in a room equipped with LED light. The thickness of all devices is 0.3 cm, while Area = L × W, whereas L = W.

illumination. With negligible deviations from simulated values, η_{opt} of LSC-1, LSC-2, and LSC-3 are found to be 12.1, 9.7, and 7.6% respectively (Table 1). On the other hand, an LSC with 2500 cm^2 area (G = 42) displays the η_{opt} 2.6% and C* is 1.06 lower than less than that under AM 1.5G illumination (2.8%, 1.17 respectively). The difference in the optical performance is attributed to the varied absorption efficiency of 4CzIPN in AM 1.5G and LED illuminations. Photostability analysis was done to suggest the applicability of our device for a long time. For this purpose, highly intense 360 nm UV light with the power of 100 mW cm^{-2} was used to irradiate the samples. Surprisingly, only a 7% decrease in emission intensity was observed after 5 h (Fig. S5). The results are explained based on strong steric hindrance occurred in 4CzIPN that avoid its photodegrading. Considering these features, TADF dyes LSC can be employed to fabricate tandem LSC-with the bottom layer having conventional dyes or quantum dots. This strategy can help to improve the overall performance of the system with the least compromise on system stability.

Most of the LSC research focuses on improving efficiency while neglecting the aesthetic and visual comfort parameters of LSCs. Nevertheless, for the practical implementation of the LSCs in the architectural environment (e.g., building windows and facades), aesthetics is just as important as efficiency [60]. Key figure-of-merits to quantify the visual performance of LSC device are chromaticity coordinates (CIE 1931 x,y and CIE Lab) of transmitted light, color rendering index (CRI) of transmitted light, and average visible transmission (AVT) [61,62]. To address the potential of the 4CzIPN-doped LSCs, we compared the visual performance of our devices with those based on Red 305 dye which is one of the most common dyes employed in LSC research [63]. The chromaticity diagram in Fig. 6a quantifies the rendered color fidelity of the light transmitted through LSC devices. As evident from Fig. 6a, the x and y coordinates of Red305-doped LSC are 0.564 and 0.185. For the 4CzIPN--doped LSC, x and y coordinates (x 0.340, y 0.441) give green tint and lie near to the coordinates of AM 1.5G illumination (x 0.332, y 0.343). Preference of the 4CzIPN-doped LSC over the Red305-doped LSC as an architectural element is endorsed by its coordinates distance from that of AM 1.5G illumination. Table 2 represents the CIELab color coordinates of LSC devices calculated using the method reported by C. Yang et al. Since 4CzIPN absorbs UV and blue parts of the visible spectrum and emits in the green region, the 4CzIPN-doped LSC has negative values of a* and positive value of b*. On contrary, Red 305 with the absorption that broadly spans the major portion of the visible spectrum (400–600 nm) and the emission, the red region leads to the positive values of a* and negative value of b*. The analysis is further supported by the spectral power distribution (SPD) of light transmitted by these devices. Fig. 6b depicts the transmitted SPD of the LSC devices which use the Red305 dyes and 4CzIPN, with the grey area in the background corresponds to the AM1.5G light transmitted through undoped PMMA plate. Transmitted SPD for both LSCs devices depends on their absorption spectra. For example, the transmitted SPD for 4CzIPN-LSC is associated with almost zero UV and blue components. Further, we extend the analysis of our devices by measuring CRI and AVT according to the method reported by C. Yang et al. [62]. CRI and AVT are key metrics to quantify the overall level of visual comfort provided by the illumination source and can be applied to evaluate perceptible color-tinting of LSC windows. Typically, CRI and AVT should be above 75 to carry the normal tasks in the given environment [64]. As can be seen in Fig. 6c, CRI and AVT of Red 305 based LSC are 51 and 17%, respectively. On the other hand, with CRI and AVT of 76 and

Table 2
CIELab parameters of LSCs.

Sample	L	a*	b*
4CzIPN-LSC	96.1	−16.0	48.1
Red305-LSC	47.2	66.5	−14.3

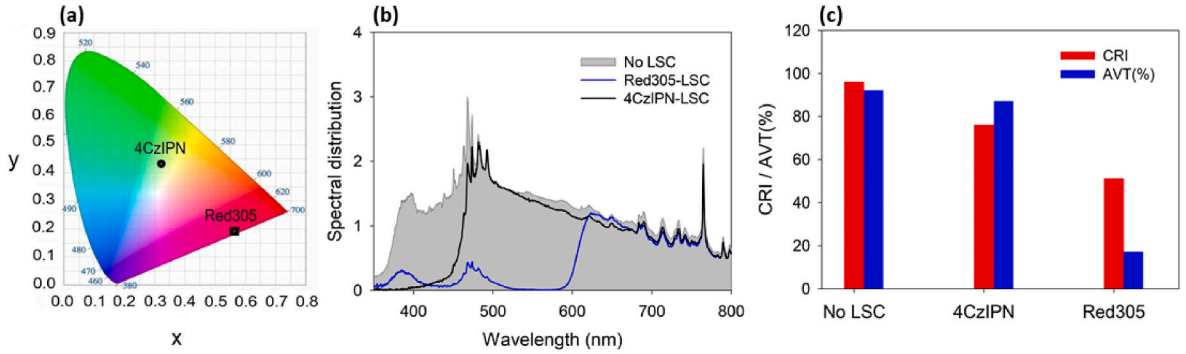

Fig. 6. (a) CIE 1931 coordinates (b) Spectral power distribution (c) CRI and AVT(%) of 4CzIPN and Red305 doped LSCs.

87%, 4CzIPN-LSC offers a better level of color neutrality and color-rendering properties, thus making itself a better option for building applications as compared to Red305-doped LSC windows.

4. Conclusion and future prospective

We presented a large-area LSC based on 4CzIPN, a D-A luminophore with large Stokes shift due to intramolecular charge transfer characteristics. A large gap between absorption and emission spectra of 4CzIPN helped to reduce the reabsorption losses significantly. As a result, the large-area LSC (400 cm^2, G = 16.6) exhibit η_{opt} as high as 5.5% (with backside diffuser) under AM 1.5G and a high degree of transparency across the visible spectrum (AVT 87%), which renders them good candidates for the realization of BIPV elements such as solar windows. We also obtained the η_{opt} of our device under indoor illumination. For this purpose, we employed a white LED (1000 lux) and obtained the η_{opt} of 7.6%. Using monte Carlo ray-tracing simulations, we further obtained the optical performances of the LSCs for the increasing area (up to 2500 cm^2, G = 42).

4CzIPN belongs to the novel class of highly efficient thermally activated delayed fluorescent (TADF) dyes that are already proved as the blockbuster emitters for organic LEDs and have excellent photoluminescent properties. There still exists a large window to improve the performance of TADF dyes based LSC devices. For example, reabsorption losses in an LSC greatly depend on the concentrations of luminophores, therefore, TADF dyes exhibiting aggregation-induced emission (AIE) hold a great potential to avoid concentration quenching and efficiency roll-off caused by the spectral overlap. TADF dyes with donor-spacer-acceptor also allow many degrees of freedom to dihedrals, valence angles, and bond lengths. All these features help to improve stability and to control the emission color of the LSC and other semi-transparent PV devices.

Author statement

The key points of the article are, **1)** To fill a gap between basic research and practical implementation, we firstly report the indoor and outdoor performance of large-area ($\geq$100 cm^2) LSCs containing a large Stokes shift donor-acceptor luminophore, 1,2,3,5 tetrakis(carbazol-9-yl)-4,6-dicyanobenzene (4CzIPN). Nearly no reabsorption loss, high photostability due to strong steric hindrance, and high photoluminescence quantum yield of 4CzIPN makes it an excellent candidate for the development of large-area LSCs. Our champion LSC device (400 cm^2) exhibits optical efficiency of 5.5% and 7.6% under solar (AM 1.5G) and indoor (white LED) illuminations, respectively. **2)** Using monte Carlo ray-tracing simulations, we further obtained the optical performances of the 4CzIPN-doped LSCs for the increasing area (up to 2500 cm^2, G = 42). **3)** The aesthetic and visual comfort parameters such as chromaticity coordinates, color rendering index, and average visible transmission of 4CzIPN-doped LSC were reported that showed that fabricated devices are aesthetically feasible for use in built environment.

Declaration of competing interest

The authors declare that they have no known competing financial interests or personal relationships that could have appeared to influence the work reported in this paper.

Acknowledgments

This work was supported by the National Research Foundation of the Republic of Korea (NRF) grant funded by the Korea government (MSIT) (No.2019R1A2C1005805) and was supported by the Korea Institute of energy technology evaluation and planning (KETEP) and the ministry of trade, industry & energy (MOTIE) of the Republic of Korea (No.20194030202320).

Appendix A. Supplementary data

Supplementary data to this article can be found online at https://doi.org/10.1016/j.jlumin.2020.117837.

References

[1] M.G. Debije, P.P. Verbunt, Thirty years of luminescent solar concentrator research: solar energy for the built environment, Advanced Energy Materials 2 (2012) 12–35.
[2] A. Hermann, Luminescent solar concentrators—a review, Sol. Energy 29 (1982) 323–329.
[3] F. Mateen, H. Oh, W. Jung, M. Binns, S.-K. Hong, Metal nanoparticles based stack structured plasmonic luminescent solar concentrator, Sol. Energy 155 (2017) 934–941.
[4] F. Mateen, M. Ali, S.Y. Lee, S.H. Jeong, M.J. Ko, S.-K. Hong, Tandem structured luminescent solar concentrator based on inorganic carbon quantum dots and organic dyes, Sol. Energy 190 (2019) 488–494.
[5] H. Li, K. Wu, J. Lim, H.-J. Song, V.I. Klimov, Doctor-blade deposition of quantum dots onto standard window glass for low-loss large-area luminescent solar concentrators, Nature Energy 1 (2016) 16157.
[6] F. Meinardi, S. Ehrenberg, L. Dhamo, F. Carulli, M. Mauri, F. Bruni, R. Simonutti, U. Kortshagen, S. Brovelli, Highly efficient luminescent solar concentrators based on earth-abundant indirect-bandgap silicon quantum dots, Nat. Photon. 11 (2017) 177.
[7] F. Mateen, H. Oh, J. Kang, S.Y. Lee, S.-K. Hong, Improvement in the performance of luminescent solar concentrator using array of cylindrical optical fibers, Renew. Energy 138 (2019) 691–696.
[8] T. Saraidarov, V. Levchenko, A. Grabowska, P. Borowicz, R. Reisfeld, Non-self-absorbing materials for luminescent solar concentrators (LSC), Chem. Phys. Lett. 492 (2010) 60–62.
[9] N.D. Bronstein, Y. Yao, L. Xu, E. O'Brien, A.S. Powers, V.E. Ferry, A.P. Alivisatos, R. G. Nuzzo, Quantum dot luminescent concentrator cavity exhibiting 30-fold concentration, ACS Photonics 2 (2015) 1576–1583.
[10] N.C. Giebink, G.P. Wiederrecht, M.R. Wasielewski, Resonance-shifting to circumvent reabsorption loss in luminescent solar concentrators, Nat. Photon. 5 (2011) 694.
[11] G. Griffini, L. Brambilla, M. Levi, M. Del Zoppo, S. Turri, Photo-degradation of a perylene-based organic luminescent solar concentrator: molecular aspects and device implications, Sol. Energy Mater. Sol. Cell. 111 (2013) 41–48.
[12] G. Griffini, M. Levi, S. Turri, Novel high-durability luminescent solar concentrators based on fluoropolymer coatings, Prog. Org. Coating 77 (2014) 528–536.
[13] A. Mansour, Photostability and optical parameters of copolymer styrene/MMA as a matrix for the dyes used in fluorescent solar collectors, Polym. Test. 23 (2004) 247–252.
[14] P. Moraitis, R. Schropp, W. Van Sark, Nanoparticles for luminescent solar concentrators-a review, Opt. Mater. 84 (2018) 636–645.
[15] J. Drake, M. Lesiecki, J. Sansregret, W. Thomas, Organic dyes in PMMA in a planar luminescent solar collector: a performance evaluation, Appl. Optic. 21 (1982) 2945–2952.
[16] I. Coropceanu, M.G. Bawendi, Core/shell quantum dot based luminescent solar concentrators with reduced reabsorption and enhanced efficiency, Nano Lett. 14 (2014) 4097–4101.
[17] H.Y. Huang, K.B. Cai, Y.R. Sie, K. Li, J.M. Yeh, C.T. Yuan, Eco-Friendly, high-loading luminescent solar concentrators with concurrently enhanced optical density and quantum yields while without sacrificing edge-emission efficiency, Solar RRL 3 (2019) 1800347.
[18] S. Peeters, Reabsorption losses in luminescent solar concentrators, Door Masterproef ingediend tot het behalen van de academische graad van, Master in de ingenieurswetenschappen: fotonica, Academiejaar, Ghent, Belgium, 2011.
[19] Y. Li, J. Olsen, K. Nunez-Ortega, W.-J. Dong, A structurally modified perylene dye for efficient luminescent solar concentrators, Sol. Energy 136 (2016) 668–674.
[20] A. Pucci, Luminescent solar concentrators based on aggregation induced emission, Isr. J. Chem. 58 (8) (2018) 837–844.
[21] J.L. Banal, K.P. Ghiggino, W.W. Wong, Efficient light harvesting of a luminescent solar concentrator using excitation energy transfer from an aggregation-induced emitter, Phys. Chem. Chem. Phys. 16 (2014) 25358–25363.
[22] M.J. Currie, J.K. Mapel, T.D. Heidel, S. Goffri, M.A. Baldo, High-efficiency organic solar concentrators for photovoltaics, Science 321 (2008) 226–228.
[23] B. Balaban, S. Doshay, M. Osborn, Y. Rodriguez, S.A. Carter, The role of FRET in solar concentrator efficiency and color tunability, J. Lumin. 146 (2014) 256–262.
[24] F. Mateen, H. Oh, W. Jung, S.Y. Lee, H. Kikuchi, S.-K. Hong, Polymer dispersed liquid crystal device with integrated luminescent solar concentrator, Liq. Cryst. 45 (2018) 498–506.
[25] R. Turrisi, A. Sanguineti, M. Sassi, B. Savoie, A. Takai, G.E. Patriarca, M. M. Salamone, R. Ruffo, G. Vaccaro, F. Meinardi, Stokes shift/emission efficiency trade-off in donor–acceptor perylenemonoimides for luminescent solar concentrators, J. Mater. Chem. 3 (2015) 8045–8054.
[26] B. Zhang, P. Zhao, L.J. Wilson, J. Subbiah, H. Yang, P. Mulvaney, D.J. Jones, K. P. Ghiggino, W.W. Wong, High-performance large-area luminescence solar concentrator incorporating a donor–emitter fluorophore system, ACS Energy Letters 4 (2019) 1839–1844.

[27] Y. Zhou, D. Benetti, X. Tong, L. Jin, Z.M. Wang, D. Ma, H. Zhao, F. Rosei, Colloidal carbon dots based highly stable luminescent solar concentrators, Nanomater. Energy 44 (2018) 378–387.
[28] F. Mateen, M. Ali, H. Oh, S.-K. Hong, Nitrogen-doped carbon quantum dot based luminescent solar concentrator coupled with polymer dispersed liquid crystal device for smart management of solar spectrum, Sol. Energy 178 (2019) 48–55.
[29] C. Yang, J. Zhang, W.-T. Peng, W. Sheng, D. Liu, P.S. Kuttipillai, M. Young, M. R. Donahue, B.G. Levine, B. Borhan, Impact of Stokes shift on the performance of near-infrared harvesting transparent luminescent solar concentrators, Sci. Rep. 8 (2018) 16359.
[30] J. Liang, C. Huang, X. Gong, Silicon nanocrystals and their composites: syntheses, fluorescence mechanisms, and biological applications, ACS Sustain. Chem. Eng. 7 (2019) 18213–18227.
[31] W. Ma, W. Li, R. Liu, M. Cao, X. Zhao, X. Gong, Carbon dots and AIE molecules for highly efficient tandem luminescent solar concentrators, Chem. Commun. 55 (2019) 7486–7489.
[32] H. Zhao, D. Benetti, X. Tong, H. Zhang, Y. Zhou, G. Liu, D. Ma, S. Sun, Z.M. Wang, Y. Wang, Efficient and stable tandem luminescent solar concentrators based on carbon dots and perovskite quantum dots, Nanomater. Energy 50 (2018) 756–765.
[33] L. Zdražil, S. Kalytchuk, K. Holá, M. Petr, O. Zmeškal, Š. Kment, A.L. Rogach, R. Zbořil, A carbon dot-based tandem luminescent solar concentrator, Nanoscale 12 (2020) 6664–6672.
[34] K. Wu, H. Li, V.I. Klimov, Tandem luminescent solar concentrators based on engineered quantum dots, Nat. Photon. 12 (2018) 105.
[35] P.T. Albers, C.W. Bastiaansen, M.G. Debije, Dual waveguide patterned luminescent solar concentrators, Sol. Energy 95 (2013) 216–223.
[36] N.J. Davis, R.W. MacQueen, S.T. Jones, C. Orofino-Pena, D. Cortizo-Lacalle, R. G. Taylor, D. Credgington, P.J. Skabara, N.C. Greenham, Star-shaped fluorene–BODIPY oligomers: versatile donor–acceptor systems for luminescent solar concentrators, J. Mater. Chem. C 5 (2017) 1952–1962.
[37] A. Kaniyoor, B. McKenna, S. Comby, R.C. Evans, Design and response of high-efficiency, planar, doped luminescent solar concentrators using organic–inorganic Di-Ureasil waveguides, Advanced Optical Materials 4 (2016) 444–456.
[38] Y. Li, P. Miao, W. Zhou, X. Gong, X. Zhao, N-doped carbon-dots for luminescent solar concentrators, J. Mater. Chem. 5 (2017) 21452–21459.
[39] Z. Wang, X. Zhao, Z. Guo, P. Miao, X. Gong, Carbon dots based nanocomposite thin film for highly efficient luminescent solar concentrators, Org. Electron. 62 (2018) 284–289.
[40] L.H. Slooff, E.E. Bende, A.R. Burgers, T. Budel, M. Pravettoni, R.P. Kenny, E. D. Dunlop, A. Büchtemann, A luminescent solar concentrator with 7.1% power conversion efficiency, Phys. Status Solidi Rapid Res. Lett. 2 (2008) 257–259.
[41] L. Desmet, A. Ras, D. De Boer, M. Debije, Monocrystalline silicon photovoltaic luminescent solar concentrator with 4.2% power conversion efficiency, Optic Lett. 37 (2012) 3087–3089.
[42] F. Meinardi, H. McDaniel, F. Carulli, A. Colombo, K.A. Velizhanin, N.S. Makarov, R. Simonutti, V.I. Klimov, S. Brovelli, Highly efficient large-area colourless luminescent solar concentrators using heavy-metal-free colloidal quantum dots, Nat. Nanotechnol. 10 (2015) 878–885.
[43] S. Li, H. Liu, W. Chen, Z. Zhou, D. Wu, R. Lu, B. Zhao, J. Hao, L. Yang, H. Yang, Low reabsorption and stability enhanced luminescent solar concentrators based on silica encapsulated quantum rods, Sol. Energy Mater. Sol. Cell. 206 (2020) 110321.
[44] M.R. Bergren, N.S. Makarov, K. Ramasamy, A. Jackson, R. Guglielmetti, H. McDaniel, High-performance CuInS2 quantum dot laminated glass luminescent solar concentrators for windows, ACS Energy Letters 3 (2018) 520–525.
[45] H. Zhao, G. Liu, S. You, F.V. Camargo, M. Zavelani-Rossi, X. Wang, C. Sun, B. Liu, Y. Zhang, G. Han, Gram-scale synthesis of carbon quantum dots with a large Stokes shift for the fabrication of eco-friendly and high-efficiency luminescent solar concentrators, Energy & Environmental Science (2020).
[46] J. Zhang, M. Wang, Y. Zhang, H. He, W. Xie, M. Yang, J. Ding, J. Bao, S. Sun, C. Gao, Optimization of large-size glass laminated luminescent solar concentrators, Sol. Energy 117 (2015) 260–267.
[47] Y. Li, Y. Sun, Y. Zhang, Luminescent solar concentrators performing under different light conditions, Sol. Energy 188 (2019) 1248–1255.
[48] F. Mateen, S.Y. Lee, S.-K. Hong, Luminescent solar concentrators based on thermally activated delayed fluorescence dyes, J. Mater. Chem. 8 (2020) 3708–3716.
[49] B.C. Rowan, L.R. Wilson, B.S. Richards, Advanced material concepts for luminescent solar concentrators, IEEE J. Sel. Top. Quant. Electron. 14 (2008) 1312–1322.
[50] T. Dienel, C. Bauer, I. Dolamic, D. Brühwiler, Spectral-based analysis of thin film luminescent solar concentrators, Sol. Energy 84 (2010) 1366–1369.
[51] H. Uoyama, K. Goushi, K. Shizu, H. Nomura, C. Adachi, Highly efficient organic light-emitting diodes from delayed fluorescence, Nature 492 (2012) 234–238.
[52] S. Sadeghi, H. Bahmani Jalali, R. Melikov, B. Ganesh Kumar, M. Mohammadi Aria, C.W. Ow-Yang, S. Nizamoglu, Stokes-shift-engineered indium phosphide quantum dots for efficient luminescent solar concentrators, ACS Appl. Mater. Interfaces 10 (2018) 12975–12982.
[53] R. Mori, G. Iasilli, M. Lessi, A.B. Muñoz-García, M. Pavone, F. Bellina, A. Pucci, Luminescent solar concentrators based on PMMA films obtained from a red-emitting ATRP initiator, Polym. Chem. 9 (2018) 1168–1177.
[54] D. Şahin, B. Ilan, D.F. Kelley, Monte-Carlo simulations of light propagation in luminescent solar concentrators based on semiconductor nanoparticles, J. Appl. Phys. 110 (2011), 033108.
[55] S. Woei Leow, C. Corrado, M. Osborn, M. Isaacson, G. Alers, S.A. Carter, Analyzing luminescent solar concentrators with front-facing photovoltaic cells using weighted Monte Carlo ray tracing, J. Appl. Phys. 113 (2013) 214510.
[56] J. Shu, X. Zhang, P. Wang, R. Chen, H. Zhang, D. Li, P. Zhang, J. Xu, Monte-Carlo simulations of optical efficiency in luminescent solar concentrators based on all-inorganic perovskite quantum dots, Phys. B Condens. Matter 548 (2018) 53–57.
[57] C. Papucci, T.A. Geervliet, D. Franchi, O. Bettucci, A. Mordini, G. Reginato, F. Picchioni, A. Pucci, M. Calamante, L. Zani, Green/yellow-emitting conjugated heterocyclic fluorophores for luminescent solar concentrators, Eur. J. Org Chem. (2018) 2657–2666.
[58] H. Mu, M. Yao, R. Wang, M. Qian, H. Xie, D. Wang, White organic light emitting diodes based on localized surface plasmon resonance of Au nanoparticles and neat thermally activated delayed fluorescence and phosphorescence emission layers, J. Lumin. 220 (2020) 117022.
[59] F. Mateen, M.A. Saeed, J.W. Shim, S.-K. Hong, Indoor/outdoor light-harvesting by coupling low-cost organic solar cell with a luminescent solar concentrator, Sol. Energy 207 (2020) 379–387.
[60] J. ter Schiphorst, M.L. Cheng, M. van der Heijden, R.L. Hageman, E.L. Bugg, T. J. Wagenaar, M.G. Debije, Printed luminescent solar concentrators: artistic renewable energy, Energy Build. 207 (2020) 109625.
[61] C.J. Traverse, R. Pandey, M.C. Barr, R.R. Lunt, Emergence of highly transparent photovoltaics for distributed applications, Nature Energy 2 (2017) 849–860.
[62] C. Yang, D. Liu, M. Bates, M.C. Barr, R.R. Lunt, How to accurately report transparent solar cells, Joule 3 (2019) 1803–1809.
[63] Z. Krumer, W.G. van Sark, R.E. Schropp, C. de Mello Donegá, Compensation of self-absorption losses in luminescent solar concentrators by increasing luminophore concentration, Sol. Energy Mater. Sol. Cell. 167 (2017) 133–139.
[64] F.M. Vossen, M.P. Aarts, M.G. Debije, Visual performance of red luminescent solar concentrating windows in an office environment, Energy Build. 113 (2016) 123–132.